AGU ADVANCING EARTH AND SPACE SCIENCE

JGR Space Physics

RESEARCH ARTICLE
10.1029/2022JA031202

Key Points:
- PROBA-V/EPT confirms that proton flux variations in the SAA are mainly due to losses at low *L* during solar maximum
- A splitting of the SAA is observed from 9.5 to 13 MeV corresponding to a double proton belt
- Big SEP events of June 2015 and September 2017 have small effects in the SAA that is more affected by geomagnetic storms at its outer edge

Correspondence to:
V. Pierrard,
viviane.pierrard@aeronomie.be

Citation:
Pierrard, V., Benck, S., Botek, E., Borisov, S., & Winant, A. (2023). Proton flux variations during solar energetic particle events, minimum and maximum solar activity, and splitting of the proton belt in the South Atlantic Anomaly. *Journal of Geophysical Research: Space Physics*, *128*, e2022JA031202. https://doi.org/10.1029/2022JA031202

Received 1 DEC 2022
Accepted 19 APR 2023

Author Contributions:
Conceptualization: V. Pierrard
Data curation: S. Benck
Formal analysis: S. Benck, E. Botek, S. Borisov
Funding acquisition: V. Pierrard
Investigation: V. Pierrard, S. Benck, E. Botek, A. Winant
Methodology: V. Pierrard, S. Benck
Project Administration: V. Pierrard
Software: S. Benck
Supervision: V. Pierrard
Validation: S. Benck
Writing – original draft: V. Pierrard
Writing – review & editing: S. Benck, E. Botek, S. Borisov, A. Winant

Proton Flux Variations During Solar Energetic Particle Events, Minimum and Maximum Solar Activity, and Splitting of the Proton Belt in the South Atlantic Anomaly

V. Pierrard[1,2], S. Benck[2], E. Botek[1], S. Borisov[2], and A. Winant[1,2]

[1]Space Physics and Solar Terrestrial Center of Excellence (STCE), Royal Belgian Institute for Space Aeronomy, Brussels, Belgium, [2]Center for Space Radiations, Université catholique de Louvain, Earth and Life Institute, Louvain-La-Neuve, Belgium

Abstract The analysis of the proton flux variations observed by the Energetic Particle Telescope (EPT) at energies >9.5 MeV from the launch of PROBA-V satellite on 7 May 2013 up to October 2022 shows an anti-correlation between the proton fluxes and the solar phase. At solar minimum, the fluxes are higher at low *L* corresponding to the northern border of the South Atlantic Anomaly (SAA). This solar cycle modulation of the inner belt is mainly due to losses by increased atmospheric interactions during solar maximum. Strong Solar Energetic Particle (SEP) events, like in January 2014, June 2015, and September 2017, inject energetic protons at high latitudes, but not in the inner belt where protons are trapped at long term at low L. Nevertheless, big geomagnetic storms, including those following SEP a few days after, can cause losses of protons at the outer border of the proton belt, due to magnetic field perturbations. A double peak in the proton belt is observed during long period of measurements only for the EPT channel of 9.5–13 MeV. The narrow gap between the two peaks in the inner belt is located around $L = 2$. This resembles to a splitting of the proton belt, separating the SAA into two different parts, North and South. The high-resolution measurements of PROBA-V/EPT allow the observation of small-scale structures that brings new elements to the understanding of the different source and loss mechanisms acting on the proton radiation belt at LEO.

1. Introduction

The South Atlantic Anomaly (SAA) is an area where Earth's magnetic field is particularly low. This comes from the fact that the Earth's magnetic axis is tilted with respect to the Earth's rotation axis by an angle of approximately 11° and that the axis of the magnetic idealized dipole is located some 400 km away from the Earth's center (Brekke, 2013). As a consequence, the SAA is also a region where inner radiation belt particles can mirror at lower altitudes increasing the local particle flux.

Unlike the geographic poles, Earth's magnetic poles are not fixed and tend to wander over time, and in parallel, the intensity of Earth's magnetic field is varying over time, for example, presently decreasing (Brekke, 2013). Hence the SAA has been drifting and growing in recent years (Amit et al., 2021; Anderson et al., 2018; Stassinopoulos et al., 2015), and those secular trends have an effect on the inner belt, especially as observed at Low Earth Orbit (LEO) (Girgis et al., 2021).

In addition to secular drifts, the inner belt particles are affected by solar cycle variation. In fact, the low-altitude geomagnetically trapped population is known to be coupled to the atmospheric density through changes induced by solar activity (Anderson et al., 2018; Bruno et al., 2021b). Protons with energies above a few tens of MeV mostly originate through the Cosmic-Ray Albedo Neutron Decay (CRAND) mechanism. Because the CRAND source comes mostly from low geomagnetic latitudes due to high cutoff rigidities, the solar modulation of the cosmic rays has a relatively small effect on the variability of the trapped protons (Bruno et al., 2021b). The major variations are due to the atmospheric loss processes, including ionization and scattering of neutral and ionized atoms, induced by solar extreme ultraviolet (EUV) radiation heating the Earth's upper atmosphere. In fact, increased EUV during solar maxima leads to higher neutral and ionospheric densities, causing a decrease of proton fluxes concentrated at low altitudes and *L* shells.

One of the particularities of the particle fluxes at low altitudes is that the high-energy trapped proton fluxes are strongly anisotropic, that is, the proton fluxes depend on their arrival direction in the plane perpendicular to the local magnetic field vector as well as on their pitch angle (angle between their velocity vector and

Table 1
Energy Ranges Corresponding to Each Resolved Virtual Channel for Protons of the EPT Instrument

Energy channel number	Protons (MeV)
1	9.5–13
2	13–29
3	29–61
4	61–92
5	92–126
6	126–155
7	155–182
8	182–205
9	205–227
10	227–248

the local magnetic field vector). The anisotropy manifests itself through a steep pitch angle distribution and the so-called East-West effect (Borisov et al., 2014; Kruglanski, 1996). The pitch angle distribution is due to the particle gyration around magnetic field lines and their mirroring in an inhomogeneous magnetic field. The East-West asymmetry is caused by the finite size of the proton gyroradius and the result of the interaction of the protons with the Earth's magnetosphere. Below 2,000 km, the gyroradii of trapped protons with energies >1 MeV are comparable to the neutral atmospheric scale height. The scale height represents the vertical distance above a planet's surface at which the density or the atmospheric pressure decreases by an exponential factor of $e = 2.718$. This means that during a gyration, the protons encounter different atmospheric densities, causing differences up to an order of magnitude for fluxes arriving from different azimuths (Bruno et al., 2021a).

Due to all those particularities mentioned here above, studying proton fluxes in the SAA is very complex. Many parameters need to be taken into account: proton energy, local position, pitch angle, East-West looking direction, solar activity level, solar cycle phase and external sporadic disturbances such as geomagnetic storms or solar energetic particle (SEP) events. When analyzing high energy proton data from instruments at LEO, it is important to take those parameters into account like, for example, in Siegl et al. (2010).

In the present work, we revisit the different features of the proton population through analysis of the EPT proton flux variations over time for different energy ranges. Section 2 briefly presents the EPT instrument and Section 3 the time evolution of proton fluxes since PROBA-V/EPT launch and the penetration of energetic protons at high L during SEP events. Yearly changes due to solar cycle are analyzed using maps of the SAA close to solar maximum and minimum in Section 4, for high energy protons including its effect on East-West asymmetry. The topic of observed effects of SEP and geomagnetic storms on the proton belt is discussed in Section 5. The existence of a double-peak structure in the inner belt for the first proton channel (9.5–13 MeV) is studied in Section 6. Finally, Section 7 discusses the results as compared with other satellite observations and conclusions are provided in Section 8.

2. The EPT Instrument

The Energetic Particle Telescope (EPT) is a charged-particle spectrometer using a stack of 12 sensor layers including in total 23 silicon detectors that allow to accumulate counts in different physical channels using information from deposited energy in the two front layers (detector S1+S3 and S2) in combination with "hit" or "not hit" information from the 10 other layers (circular detectors DAM1-DAM10 and corresponding anticoincidence rings) (Cyamukungu et al., 2014). The first layer is subdivided into a central sensor S1 (diameter 3.5 mm) surrounded by an adjacent sensor ring S3 of outer diameter 35 mm. The second layer is composed of one plane circular sensor S2. The proton flux is obtained in 10 virtual channels (there are 10 others for Helium ions and 6 for electrons) spanning the energy ranges given in Table 1. The fluxes in each virtual channel are obtained after unfolding of the measured spectra with the efficiency matrix of the detector. It is possible to unfold separately the information obtained with the S1 and S1+S3 sensors.

The EPT is accommodated on board the PROBA-V satellite launched on 7 May 2013 on a Low Earth Orbit (LEO), 820 km altitude, 98.7° inclination and a 10:30–11:30 Local Time at Descending Node (Pierrard et al., 2014). The orbital rotation period of the satellite is 101.21 min, so that it revolves 14 times around the globe in 24 hr. The opening angle of EPT, as defined by the two front sensor layers, is 52°. The EPT is installed on the satellite in such a way that the symmetry axis of the telescope is pointed East on the night side and West on the dayside (boresight orientation of the instrument along the orbit). This orientation feature of the mission allows natural regular sampling of East-West asymmetry of proton fluxes.

The angle between its boresight direction and the local magnetic field, that is, average pitch angle (PA) of sampled particles, varies usually between 60° and 120°, that is, around 90°, when no off-pointing of PROBA-V is performed for specific operational reasons or some scientific investigations as for example, proton pitch angle

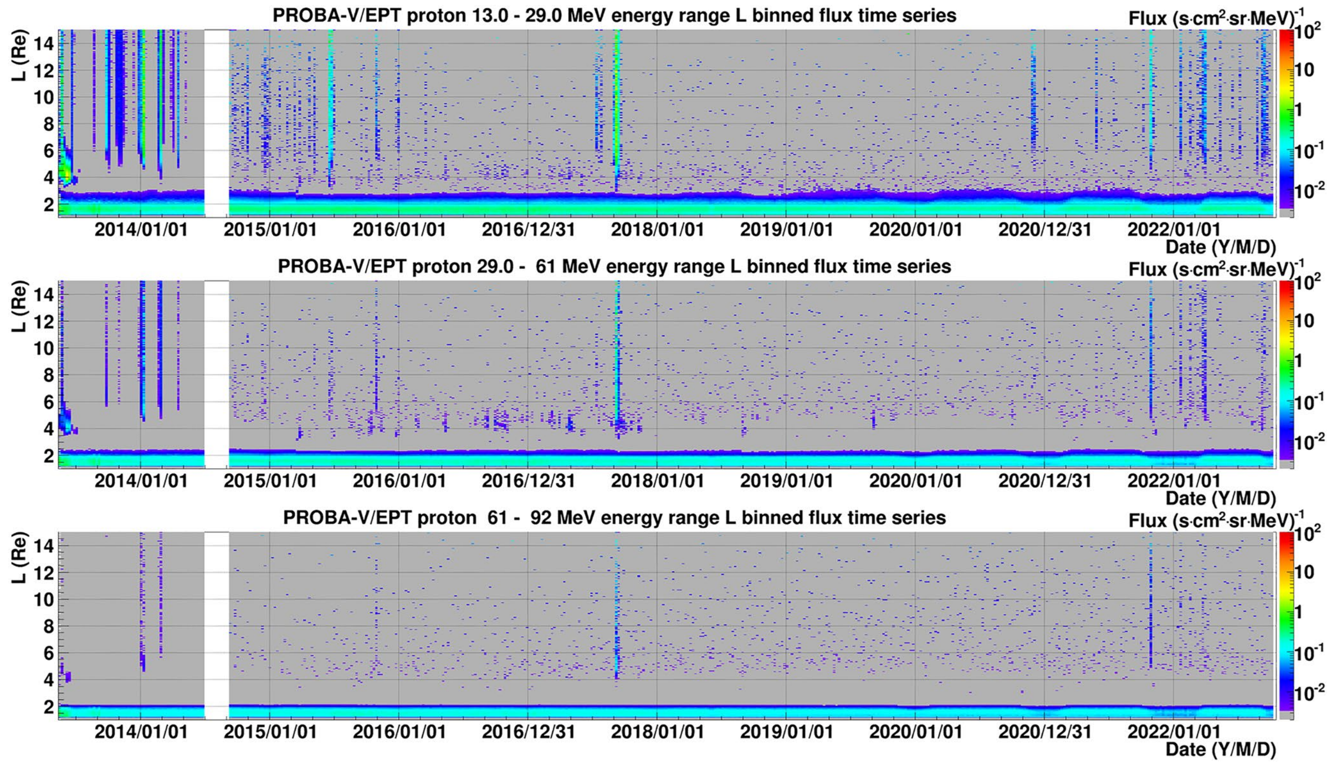

Figure 1. Proton flux (color scale) observed by EPT in Ch 2 (13–29 MeV, upper panel), Ch 3 (29–61 MeV, middle panel) and Ch 4 (61–92 MeV) (bottom panel) as a function of L and time from 7 May 2013 up to October 2022. The vertical white band in the data represents the recalibration period wherein no acceptable data was acquired. The data are averaged per week and bins of size 0.05 in L.

distribution (PAD) studies (Borisov et al., 2014). The angle between the instrument boresight direction and the local magnetic field is assumed to give the average particle pitch-angle over the field-of-view in the inertial reference system. The standard time resolution of the measurements is 2 seconds.

The position of the satellite is provided by the geographic latitude, longitude and the altitude. The McIlwain L (1966) and local B-field strength are evaluated using the UNILIB v2.20 (https://www.mag-unilib.eu/) implementation of the IGRF/Olsen-Pfitzer quiet-time magnetic field model.

Proton spectra measured by EPT have been investigated in Borisov et al. (2014), Benck et al. (2016), and Lopez Rosson and Pierrard (2017). Other previous studies of EPT data focused more on electron flux variations during geomagnetic storms (Pierrard & Lopez Rosson, 2016), especially injections of MeV electrons in the inner belt (Pierrard et al., 2019) and dropouts (Pierrard et al., 2020).

3. Time Evolution of Proton Fluxes Since PROBA-V/EPT Launch

The proton belt is much more stable than the outer (Pierrard & Lopez Rosson, 2016) and inner electron belts (Pierrard et al., 2019). Proton flux variations are slow in the inner belt, with typical time scale around years, but during very intense SEP events, energetic protons are injected at high *L* during a few days.

Figure 1 illustrates the proton flux observed by EPT from the launch on 7 May 2013 up to October 2022, for three selected channels 2, 3, and 4 of energies, 13–29 MeV, 29–61 MeV, and 61–92 MeV respectively. The 2D-histograms represent the differential proton fluxes (color scale) as a function of the McIlwain parameter *L* (*y* axis) and time (*x* axis). No EPT data are available during ~2.5 months from end June to mid-September 2014 due to a needed recalibration (Borisov & Benck, 2019), imposed by a gain change and noise increase in the S3 detection chain. This is represented on Figure 1 by the white region. As consequence, there are some restrictions as to the use of the data (latest data set available on https://swe.ssa.esa.int/space-radiation):

1. Proton channel 1 [9.5–13 MeV] is based on S1+S3 information before 27 June 2014 and on S1 data alone afterward. As the size of the S1 sensor is about 100 times smaller than the one of S3, the statistics in the

Table 2
The Most Intense Events With pfu >15,000 After Year 2000 (Line 1 to 4) Compared With Main SEP Events (With pfu >800) Observed After the Launch of EPT (Line 5 to 9)

Start date	Proton flux (pfu for $E > 10$ MeV)	Comment	Dst min (nT) in the next 3 days
14 Jul 2000	24,000	Very strong	−301 (16 Jul)
04 Nov 2001	31,700	Very strong	−292 (6 Nov)
22 Nov 2001	18,900	Very strong	−221 (24 Nov)
28 Oct 2003	29,500	Very strong	−401 (30 Oct)
22 May 2013	1,660		−27 (24 May)
6 Jan 2014	1,033		−22 (9 Jan)
21 Jun 2015	1,070		−198 (23 Jun)
5 Sep 2017	844		−122 (8 Sep)
10 Sep 2017	1,490		−34 (12 Sep)

channels defined with S1 are very low and the data can only be used within averages (e.g., integration in time) and not as individual 2 s resolution measurements. The field of view is also different which might give changes in the observed proton fluxes if the flux is highly anisotropic.

2. After June 2014, the proton channel 2 [13–29 MeV] based on S1+S3 information is highly affected by off-aperture particles and is not useable for detailed studies. This abnormality decreases strongly with energy and becomes definitively negligible for channel 5 [92–126 MeV] and higher. In the region where SEP events can be observed ($L > 3$), the lower channels are replaced by "S1-only" data in the data set with the same limitations as for channel 1 (see Jiggens et al. (2019) for an example of results obtained with averaged "S1-only" data).
3. When the flux of >1 MeV electrons is above $2{\bullet}10^3$ cm^{-2} s^{-1} sr^{-1}, electron contamination can be observed in proton channel 2 [13–29 MeV] and 3 [29–61 MeV] (see small blue vertical bands (thus not very high flux) in the $L = 4$–5 region from January 2016 to mid-2017, best visible for channel 3 (middle panel of Figure 1)).

Independent of those caveats coming from the detector itself, other features can be observed on Figure 1 coming from the orientation of the satellite. In fact, during the last winters, starting end 2019, the satellite is more often re-orientated for its proper needs in such a way that EPT's pitch angle gets far away from its nominal 90° ending up with an average lower flux in the SAA (see dips in the band $1 < L < 2.5$ representing the proton belt).

Figure 1 shows that there are proton flux injections at high L only when there are SEP events (see the vertical lines at $L > 3$, in green for the strongest events). While the geomagnetic activity is high during 2015 (Pierrard & Lopez Rosson, 2016), SEP events are observed mainly at the beginning of the EPT flight, more specifically in 2013 and 2014. Later, SEP events are more spaced in time and appear mainly in 2015 and 2017. Note that no strong SEP event occurred after September 2017 until October 2022. Very few of these SEP injections barely seem to reach the proton belt extending down to L ∼ 3 for channel 1 and at lower L for higher energies (Benck et al., 2016). Some events, especially the two biggest ones of June 2015 and September 2017, inject energetic protons to lower L than the others, and include a strong proton population with energies >13 MeV (Ch 2, upper panel). For Ch 3 (middle panel), high L injections are observed only in January 2014 and September 2017, and also on 22 May 2013 just after the launch of EPT. Since within a SEP event, the flux of protons generally strongly decreases with energy, the channels above 61 MeV (from channel 4 on) are only affected by very strong events. Note that end May 2013, the EPT was still in its commissioning phase and the energy limits for the particle classification were not fully optimized, hence the appearance of a strange shape between $L = 4$ and 5 which is due to misclassified high energy electrons. Later, after the recalibration in September 2014, such structures reappear when the fluxes for electrons with $E > 1$ MeV are above $2{\bullet}10^3$ cm^{-2} s^{-1} sr^{-1}.

We show in Table 2 the intensity (in particle flux unit (pfu) at energy >10 MeV, 1 pfu = 1 p cm^{-2} sr^{-1} s^{-1}) of the main SEP events observed during the launch of EPT and the most intense events after the year 2000 for comparison (from https://umbra.nascom.nasa.gov/SEP/). One can see that even the most intense SEP in September 2017 is very moderate in comparison to the events appeared in November 2001 and October 2003. In the past, only the very strong SEPs did highly affect the $L < 3$ region due to the injection of energetic protons (Baker et al., 2018). Note that SEP events are not always associated to geomagnetic storms: around 75% of the SEP events from 1978 to 2022 are followed by geomagnetic storms with Disturbed Storm Time index Dst < −50 nT during the next 3 days (Ameri & Valtonen, 2019), but this is not systematic, as shown in the last column of Table 2.

4. Evolution of Proton Fluxes in the SAA With the Solar Cycle

Within this section, we study the proton belt as observed by the EPT from the maximum of solar cycle 24 (in 2014) to the following minimum (in 2019) and look what changes it undergoes within this solar cycle phase during the covered time period June 2013-October 2022.

Figure 2 shows the evolution of the average monthly sunspot number from 2000 to 2022, thus including part of the solar cycle 23 and the complete solar cycle 24 that started end 2008 and ended in December 2019 (retrieved

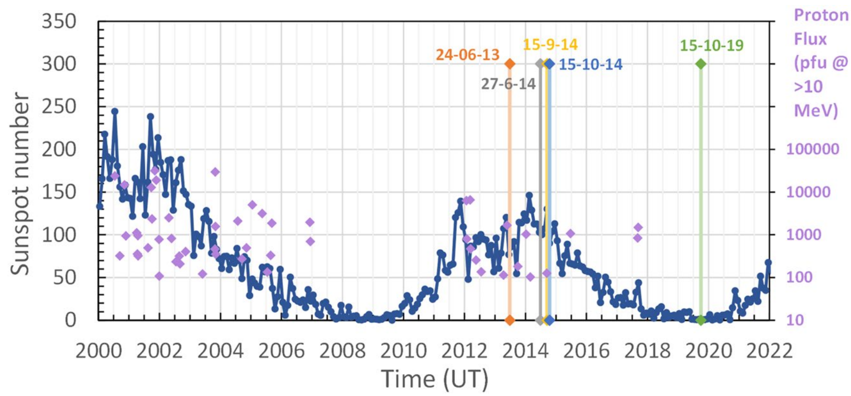

Figure 2. Monthly averaged sunspot number, as a function of time (blue dots connected by continuous blue lines). The purple diamonds show the maximum proton flux as measured by GOES spacecraft at Geosynchronous orbit during each SEP event with pfu>100, with the corresponding scale given by the axis on the right. The fluxes are integral 5-min averages for energies >10 MeV. Some important dates in the EPT data analysis are also shown (see text).

from http://www.sidc.be/silso/datafiles). It indicates that the solar activity was around maximum in 2014 and reached minimum in 2019. The purple diamonds in Figure 2 show, for listed SEP events (https://umbra.nascom.nasa.gov/SEP/), the maximum 5 min averaged proton ($E > 10$ MeV) fluxes as measured by GOES spacecraft at Geosynchronous orbit.

The nominal period for EPT data acquisition lasts from 24 June 2013 (orange) to 27 June 2014 (gray line), and corresponds to the solar maximum. Many SEP events are observed during this period of 2013–2014. The recalibration period of EPT lasted from 27 June 2014 (gray line) until 15 September 2014 (yellow line). After this period, the declining phase of solar activity started. The minimum corresponds to end 2019 (green line for 15 October 2019) with the new solar cycle 25 starting in December 2019. While many geomagnetic storms are observed during this declining period (Pierrard & Lopez Rosson, 2016), only 2 big SEP events are observed, in June 2015 and September 2017. The blue and green lines indicate the middle of two months that are selected for analysis in the next section, that is, 15 October 2014 (representative of solar maximum) and 15 October 2019 (representative of solar minimum). For these months, the geographical maps of observed EPT fluxes are drawn on Figure 3. This allows us to get a global view on the long-term variation of the proton flux trapped in the SAA at 820 km.

4.1. Geographic Maps of the Flux Variations in the SAA for Protons With $E > 60$ MeV

Figure 3 shows the proton fluxes measured by EPT Ch 5 (92–126 MeV) in the SAA, monthly averaged in bins $4° \times 4°$, for October 2014 (solar maximum) in the upper panel, for October 2019 (solar minimum) in the middle panel, and the flux ratio 2019/2014 in the bottom panel. The data is shown for night side when EPT is looking East to avoid East-West asymmetry and for boresight orientation $80° < PA < 100°$ to avoid any variation due to steep PAD. This is the reason why different areas have no measurements and are left blank. The (almost) horizontal black isolines correspond to constant L values, with low L close to the equator. The bold (almost vertical) black lines are parts of trajectories showing how EPT crosses the SAA during night passes. The pink ovals correspond to the isolines of the magnetic field (B) intensity, with low values in the center of the SAA.

From the bottom panel of Figure 3 showing the flux ratio of 2019/2014, it can be observed that the fluxes at low L (<1.22) and high B, corresponding to the northern border of the SAA, increase by a factor up to times 3 during minimum activity (see red regions). In the same way, the north eastern and western part also show flux increase, but to a lesser extent (see green regions). Thus, from 2014 to 2019, the flux increases at low L. On the contrary, in the South part of the SAA, along $L = 1.7$–2, the flux has decreased in 2019 by a factor 1.5–2 (see dark blue region). Here, it must be mentioned that all these regions include flux measurements with low statistics. However, such behavior is observed at all energies above 60 MeV, and also when other months are used provided they are spaced enough in time to make the long-term small variations visible.

From 2014 to 2019, the flux at $L < 1.25$ increases in anti-correlation with the solar activity, as shown by the red and green regions corresponding to the Northern part of the SAA. Different spectral characteristics in North and

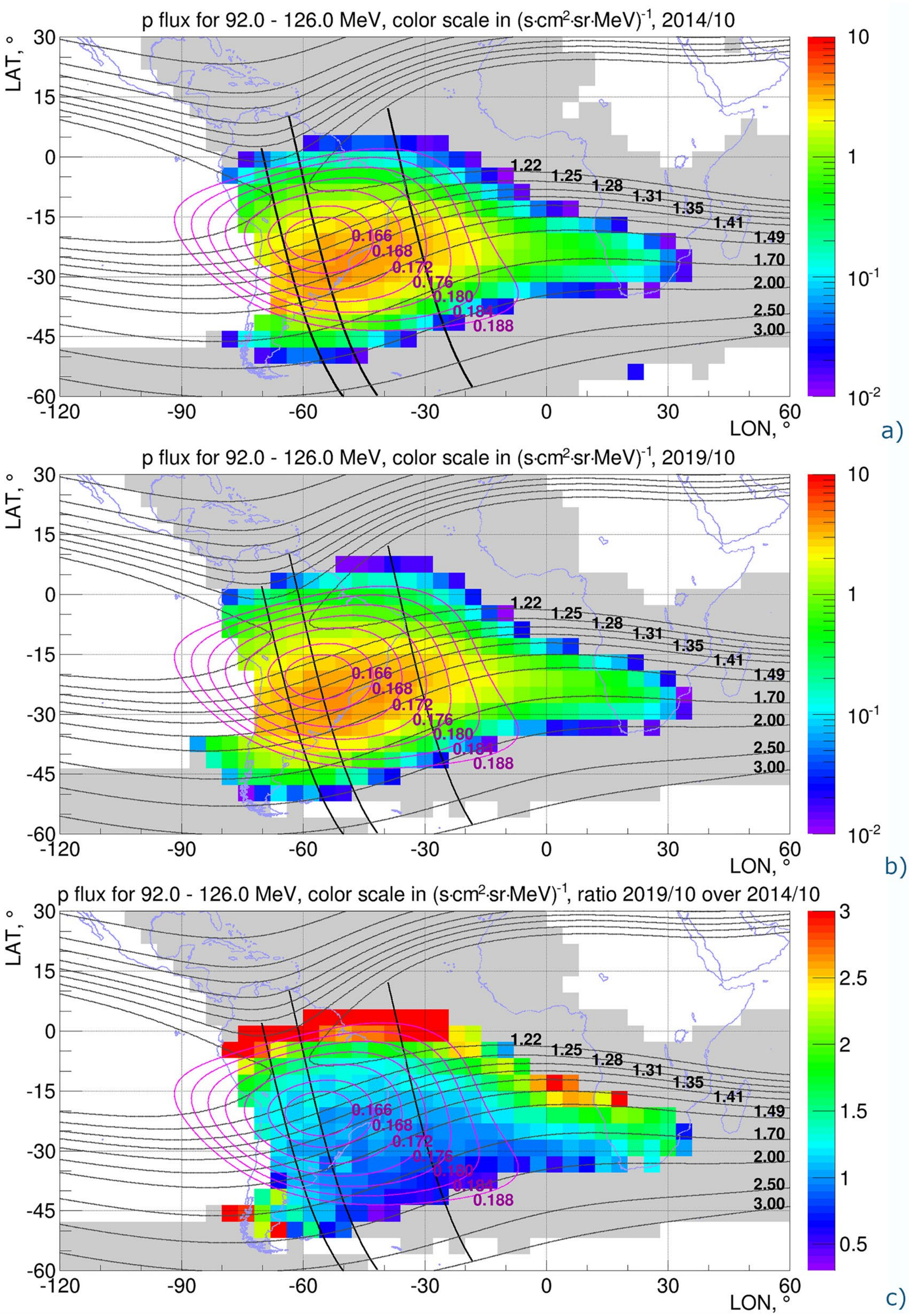

Figure 3. Geographical maps of the monthly averaged proton flux in Ch 5: (a) October 2014, (b) October 2019, (c) ratio of 2019 data divided by 2014 data. The bold black lines are parts of trajectories showing how EPT crosses the SAA during night passes from south to north. The gray areas are those where the fluxes are below minimum, that is, 10^{-2} s^{-1} cm^{-2} sr^{-1} MeV^{-1}., and the white areas are those where no data fulfill the selection criteria: night side data with boresight orientation 90° ± 10°. Iso-L lines and Iso-B lines are shown by black and pink lines respectively.

South parts of the SAA were already noted in Pierrard et al. (2014) and Lopez Rosson and Pierrard (2017), but without clear identification of the origin. The observed modulation of proton fluxes at low altitude and at low L associated to the solar cycle seems mainly due to the influence of the atmosphere. During solar maximum (in 2014), the atmosphere extends to higher altitudes and causes more important loss of protons. Atmospheric loss may thus explain the lower fluxes observed in 2014 compared to 2019.

In the region of highest L (like $L = 2$) corresponding to the outer edge of the proton belt and the South part of the SAA, the flux at lowest B for high energy protons ($E > 60$ MeV) is on the contrary showing a decreasing trend when going toward solar minimum. This may be related to geomagnetic activity and will be discussed in more details in Section 5.

The observation of the atmospheric effect is in good agreement with other long-term measurements at low-Earth orbit (LEO) like SAMPEX (Heynderickx et al., 1999; Pierrard et al., 2000) or POES (Li et al., 2020), for which clear solar cycle variations of the proton fluxes are observed and anti-correlate with the solar activity marked by the sunspot number. The atmospheric density varies with the 11-year solar cycle so that the low L proton population is lower during high solar activity. The solar cycle modulates the flux at the border of the SAA. During solar maximum, the flux decrease is mainly due to this enhanced atmospheric loss.

In addition to the lower extension of the atmosphere during solar minimum, the slow increase of radiation belt proton fluxes from 2014 to 2019 may also be influenced by CRAND (Selesnick et al., 2014). The most energetic particles of the galactic cosmic rays (GCR) interact with neutral atoms in the upper atmosphere and produce energetic albedo neutrons which decay into protons, electrons, and antineutrinos (Li et al., 2021). Because they are electrically charged, some of these electrons and protons become geomagnetically trapped at low altitude in the inner belt region. The protons retain most of the kinetic energy of the neutrons, while the electrons have lower energies (Li et al., 2017). Atmospheric neutrons generated by cosmic rays (>GeV) are detected by neutron monitors at the surface of the Earth. They show a variation of ∼20% over the 11-year solar cycle, due to the modulation of the parent cosmic rays by the solar wind. GCR are more intense during the quiet period of 2018 and 2019, so that this source mainly explains the increase of the fluxes. Nevertheless, the magnitude of the flux variation is much greater than the solar cycle variation of atmospheric neutrons that are the source of these trapped protons (Li et al., 2021), so that effects of the terrestrial atmosphere seem to dominate in the solar cycle modulation at low altitude.

4.2. Modulation With Solar Phase: Shifted Anti-Correlation

Figure 4 shows the time evolution of the flux in three bins corresponding to different parts of the SAA. Different energies are selected to show that the trend is observed over a large energy range. The first bin is located at the top border of the SAA at low $L = 1.23$ and $B = 0.18$ (top panel). The flux shows a clear anti-correlation with the solar cycle, thus is at minimum in 2014–2015 and slightly increases until 2019. The second bin is located in the center of the SAA ($L = 1.33$, $B = 0.168$) (second panel). No long-term variation is observed in this bin. The flux variations seem to be limited to the boarders of the SAA. These trends at these two locations look common to all the energy bins. At the southern border of the SAA corresponding to higher L ($L = 2.13$ in the third panel), that is, the outer boarder of the inner belt, the flux is anti-correlated with the solar cycle but with a larger time delay, the minimum being observed during a longer period than in the northern border. At high L, the flux continues to be low up to mid-2018 when it starts to increase. At this position, this trend can only be observed up to 90 MeV as the flux of the higher energies has fallen off to a level that no observations can be done. The lowest proton energy bin observed by EPT shows however a different scenario as will be shown in Section 5. So, the origin of this delayed minimum is supposed to be related to the processes involved that regulate the proton population in the inner belt and that divide the inner belt in a region where high energy protons (>60 MeV) are abundant and a region where they are absent (see Section 5). Note that here again, a selection has been made to avoid the effects of the East (night) and West (day) directions of the instrument: (a) boresight orientation, that is, PA of the viewing direction with respect to the magnetic field between 80° and 110°; (b) only night side data is included, that is, EPT is looking East. For dayside data (EPT looking West), the viewing direction of EPT does mostly not fulfill the PA condition.

4.3. Atmospheric Effect and East-West Asymmetry

Figure 5 shows maps of proton flux as a function of the invariant altitude (location of the mirror points) versus magnetic latitude for November 2014 (top panels) and October 2019 (bottom panels). This coordinate system was introduced by Cabrera and Lemaire (2007) to map the radiation belt fluxes in the low-altitude environment. Left

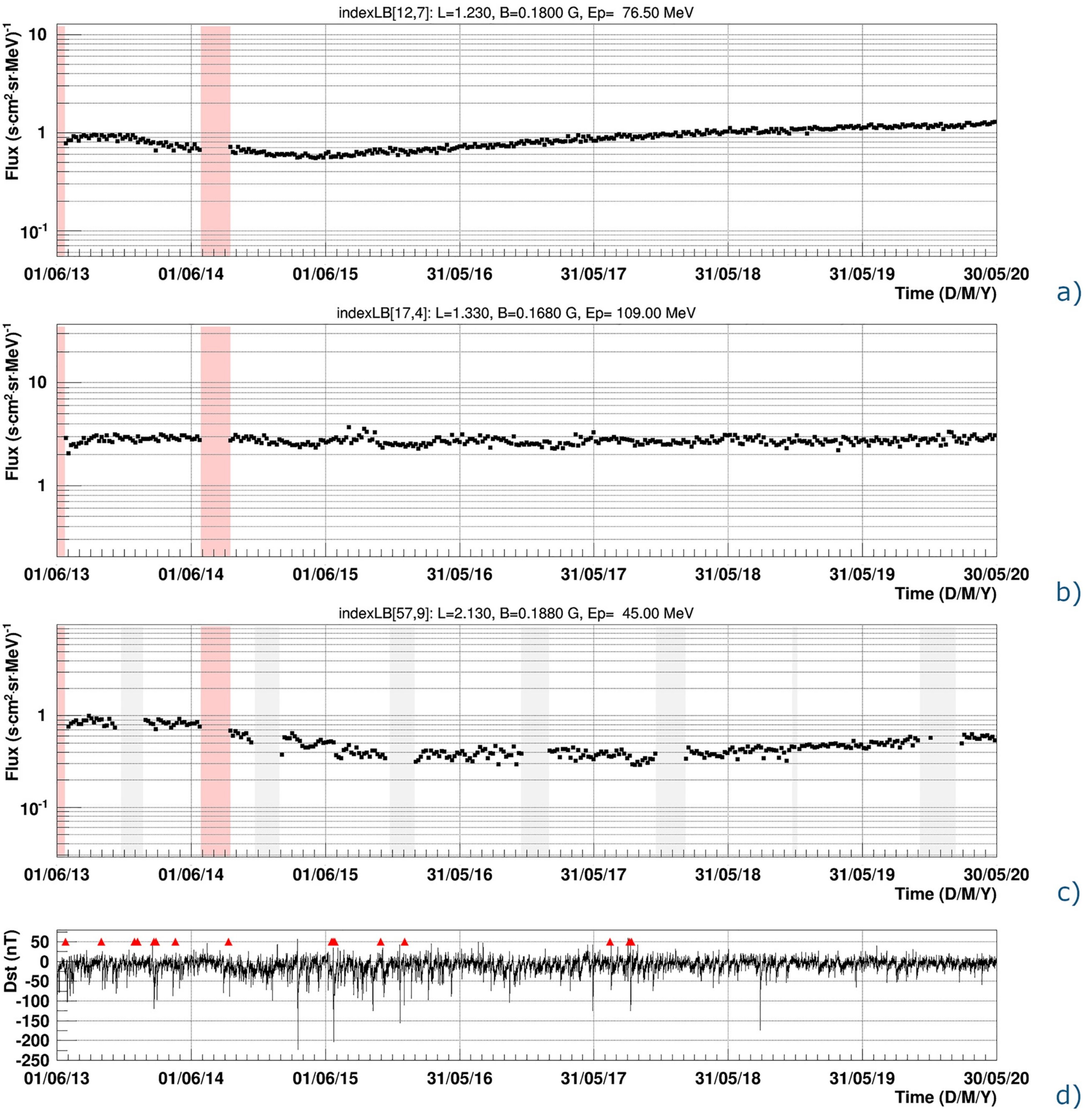

Figure 4. Time series of proton flux (weekly averages) in the SAA at three different positions for different energies. One from the northern border at low $L = 1.23$ (a), one from center at $L = 1.33$ (b) and one from the southern border at $L = 2.13$ (c). The fluxes present night-side data with boresight orientation $90° \pm 10°$. The pink bands indicate the time periods where the EPT was in its commissioning phase or recalibrated. The gray bands highlight the time periods where no data exist for the pitch angle selection. The bottom panel (d) shows Dst as a function of time and the red triangles indicate the occurrence of SEP events.

panels correspond to west direction, right panels to east direction. The figure shows that the mirror points are lower, that is, have a lower invariant altitude, when looking west and during solar minimum (bottom panels), although less pronounced. This can be observed especially for the lowest L values (see the invariant altitude line 1,200 km for instance). This illustrates that it is important to not mix east- and west-looking data for energetic protons at low orbit.

At low altitudes, the high-energy trapped proton fluxes are strongly anisotropic because they are controlled by the density distribution of the Earth's atmosphere that induces a steep pitch-angle distribution. The East-West effect caused by the finite size of the proton gyroradius was already pointed by Kruglanski (1996) for instance.

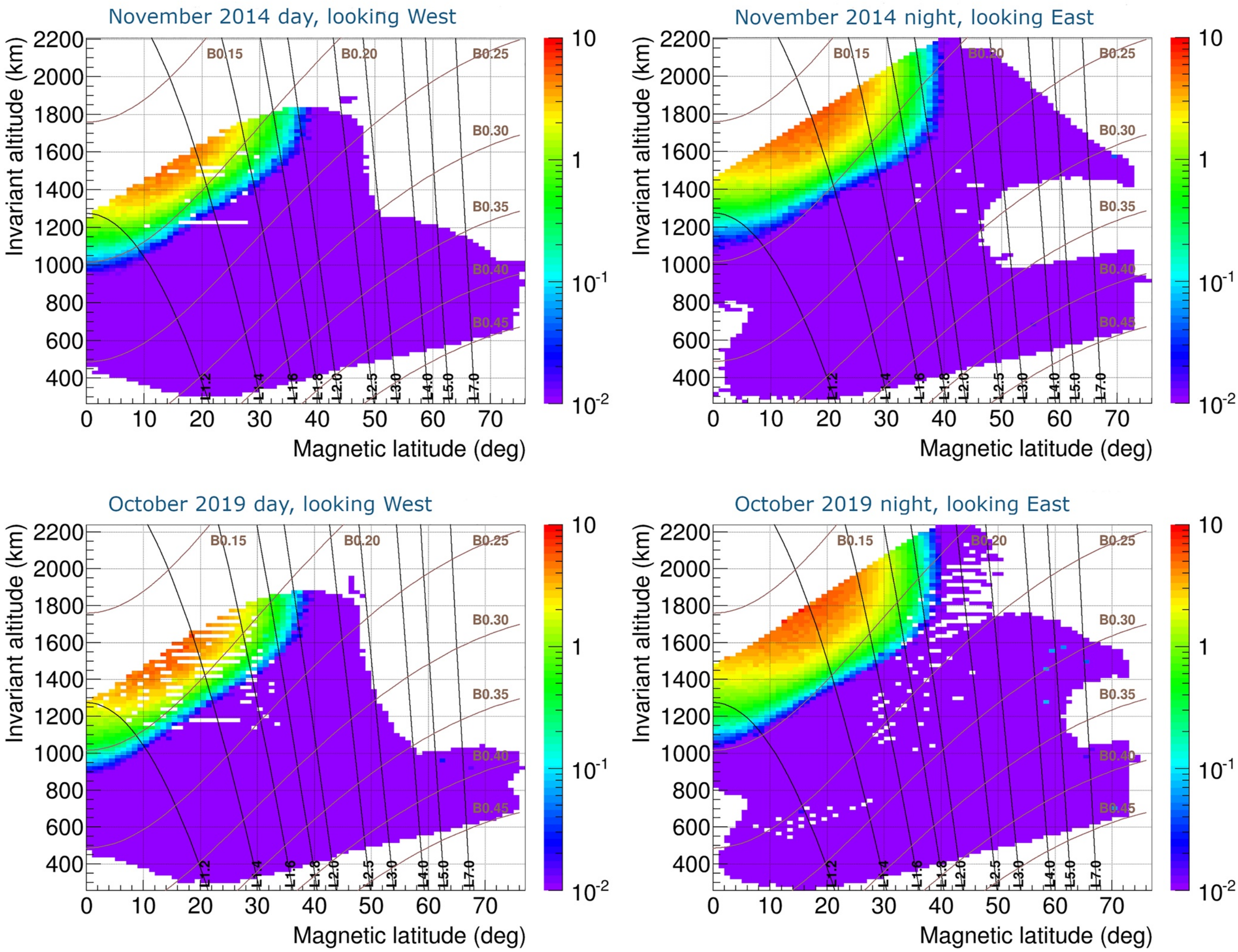

Figure 5. Invariant altitude versus magnetic latitude map for proton channel 4 [61–92 MeV]. The color scale is particle flux in s^{-1} cm^{-2} sr^{-1} MeV^{-1}. Top left panel: November 2014 day, looking West, Top right: November 2014 night, looking East, Bottom left: October 2019 day, looking West, Bottom right: October 2019 night, looking East. The isolines of L and B are also shown in black and brown respectively.

Figure 6 illustrates the averaged proton fluxes measured by the EPT as a function of B/B_0 where $B_0 = 0.311653/L^3$ (Gauss). B_0 is the magnetic field intensity at the equator of the magnetic shell L. It shows that the East-West asymmetry is strongest for low L values (top panels) and increases with energy (right panels). While for the lowest L, both regime regions (cf. blue curve with two slopes) are affected by the solar phase change, showing higher flux at solar minimum, at high L only the fluxes in the region where atmospheric interactions are dominant are significantly increased during solar minimum.

4.4. Pitch Angle Distribution

The particle flux is nominally reconstructed within the isotropic flux assumption, that is, the efficiency matrix is simulated by assuming isotropic flux at the aperture. But the higher the proton energy, the narrower the Field of View (FOV), that is, FOV = 52° as defined by the front sensor "S1+S3" and second sensor S2 (for the first channel 9.5–13 MeV) and FOV = 35° as defined by "S1+S3" and the fourth DAM (for the channel 92–126 MeV) (Cyamukungu et al., 2014).

So with EPT, especially for the high energies, the flux corresponds much closer to the $J(90°)$ flux (with $J(\alpha) = J(90°)\cdot\sin^n(\alpha)$, α is the pitch angle) rather than to omnidirectional flux, hence the higher flux levels observed.

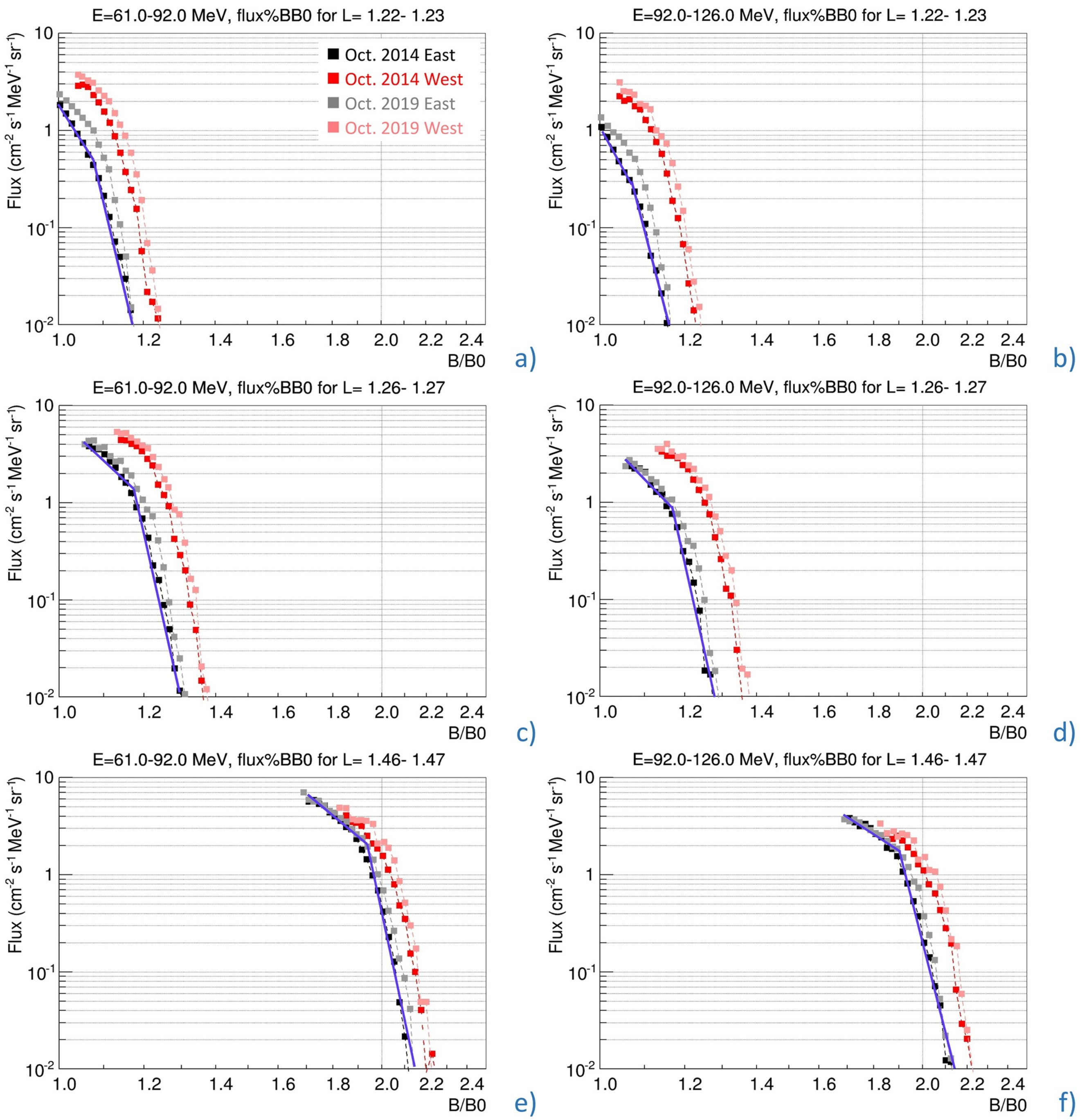

Figure 6. For two time periods (October 2014 and October 2019), for the two orientations of the satellite (West in red, East in black), averaged proton fluxes measured by the EPT in the 61–92 MeV (left panels) and 92–126 MeV (right panels) energy channel for $L = 1.22$–1.23 (top panels), $L = 1.26$–1.27 (middle panels) and $L = 1.46$–1.47 (bottom panels) as a function of B/B$_0$. The two-slopes blue line across black points (night time measurements) aims to show the two regimes of dominant proton interactions: with magnetic field (at lower B/B_0) and upper atmosphere (at higher B/B_0).

If the dominant interaction is with the magnetic field, then assuming $J(\alpha) = J_0 \sin^n(\alpha)$ for PAD (here $J_0 = J(90°)$) and $\sin^2(\alpha_0) = \sin^2(\alpha)\, B/B_0$ (where α_0 is the equatorial pitch angle), one can express the flux in this form:

$$J(\alpha) = J_0 \sin^n(\alpha_0)(B/B_0)^{-n/2}$$

The distribution of $J(\alpha)$ versus B/B_0 in log-log scale is located around a line with a slope $-n/2$, for instance on Figure 6, this corresponds to the slope of the left part of the blue curves. The n values obtained here are of

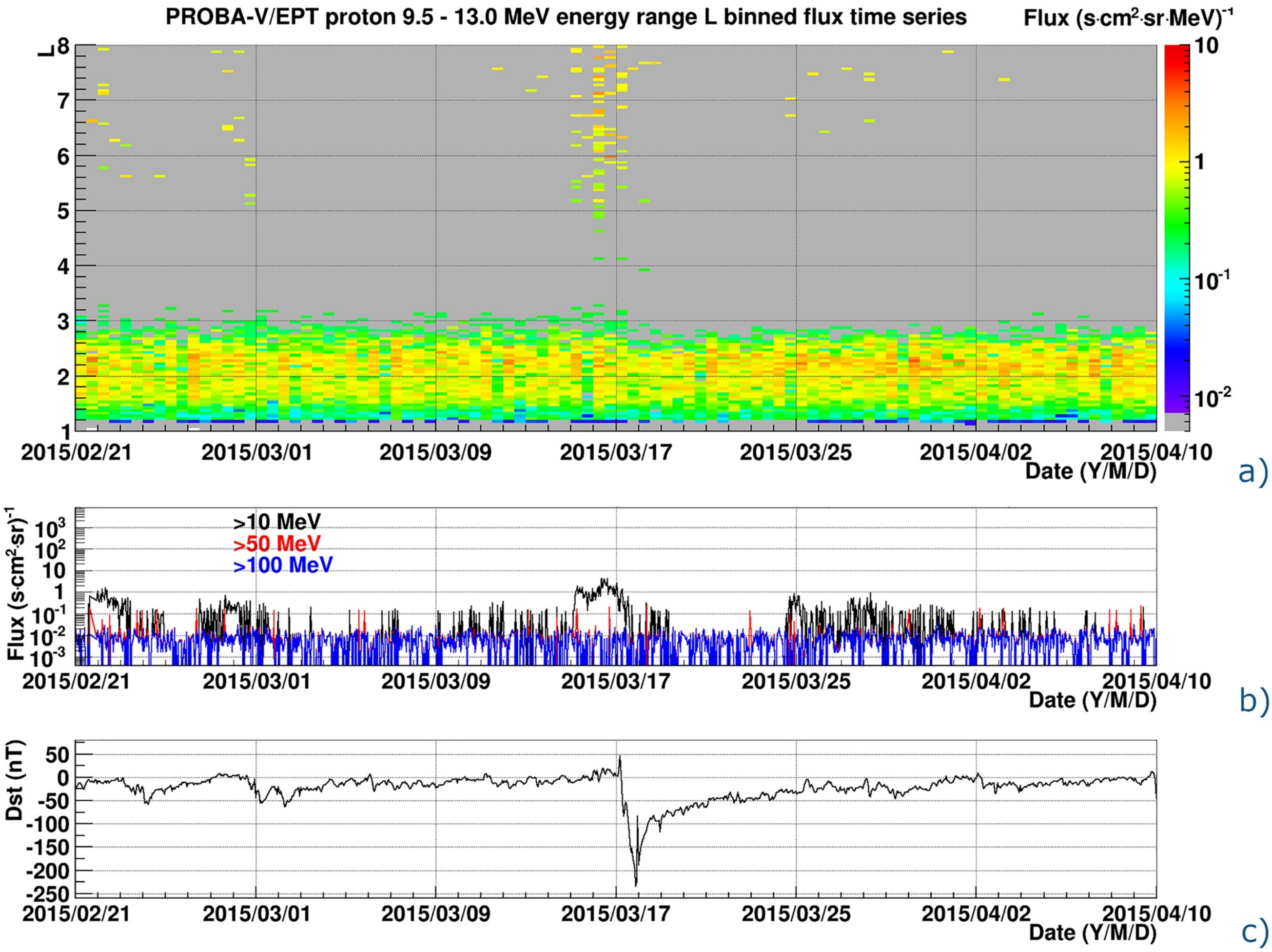

Figure 7. (a) Proton differential flux observed by EPT in Ch 1 (9.5–13 MeV) as a function of L and time from 21 February to 11 April 2015 (upper panel). The bin size in L is 0.05 and the bin size in time is 0.5 day. (b) The EPT derived integral fluxes for protons of $E > 10$ (black), >50 (red), and >100 MeV (blue) for the same time period. (c) Dst variation showing the up-to-now largest Dst decrease during PROBA-V mission.

the order of 20 but with very high uncertainty. Given the imprecision that arises from this method, it was not possible to perform any study of change in PAD with the solar cycle. A detailed study of PAD based on targeted re-orientation of the satellite in 2014 can be found in Borisov et al. (2014).

5. Effects of SEP and Geomagnetic Storms

Within this section, we revisit the proton population as observed by EPT from June 2013 to October 2022 and look at how the proton belt is affected by geomagnetic activity and SEP events during that time period.

Geomagnetic storms following SEP may have an effect on the outer edge of the proton belt, as it can be observed in Figure 7 (see upper panel) which shows proton data during the strongest geomagnetic storm (Pierrard & Lopez Rosson, 2016) of solar cycle 24, appearing on 17 March 2015, reaching a Dst index of −223 nT (Figure 7c, Dst data retrieved from https://wdc.kugi.kyoto-u.ac.jp/). One can see in Figure 7a that it is associated to a SEP event of small intensity arriving a few days before and injecting protons of $E < 50$ MeV at high L. The data from Figure 7b represent pass-averaged flux time series derived from EPT, a pass starting when $L > 6$ over a polar region (data downloaded from https://swe.ssa.esa.int/space-radiation). This event was not reported as a SEP event (on https://umbra.nascom.nasa.gov/SEP/), because the flux is lower than the threshold of 10 $p^+ cm^{-2} s^{-1} sr^{-1}$ that has been chosen to register the SEP event within the database. In fact, it appears as very faint event in Figure 7a as compared to other SEP events appearing during the flight of PROBA-V.

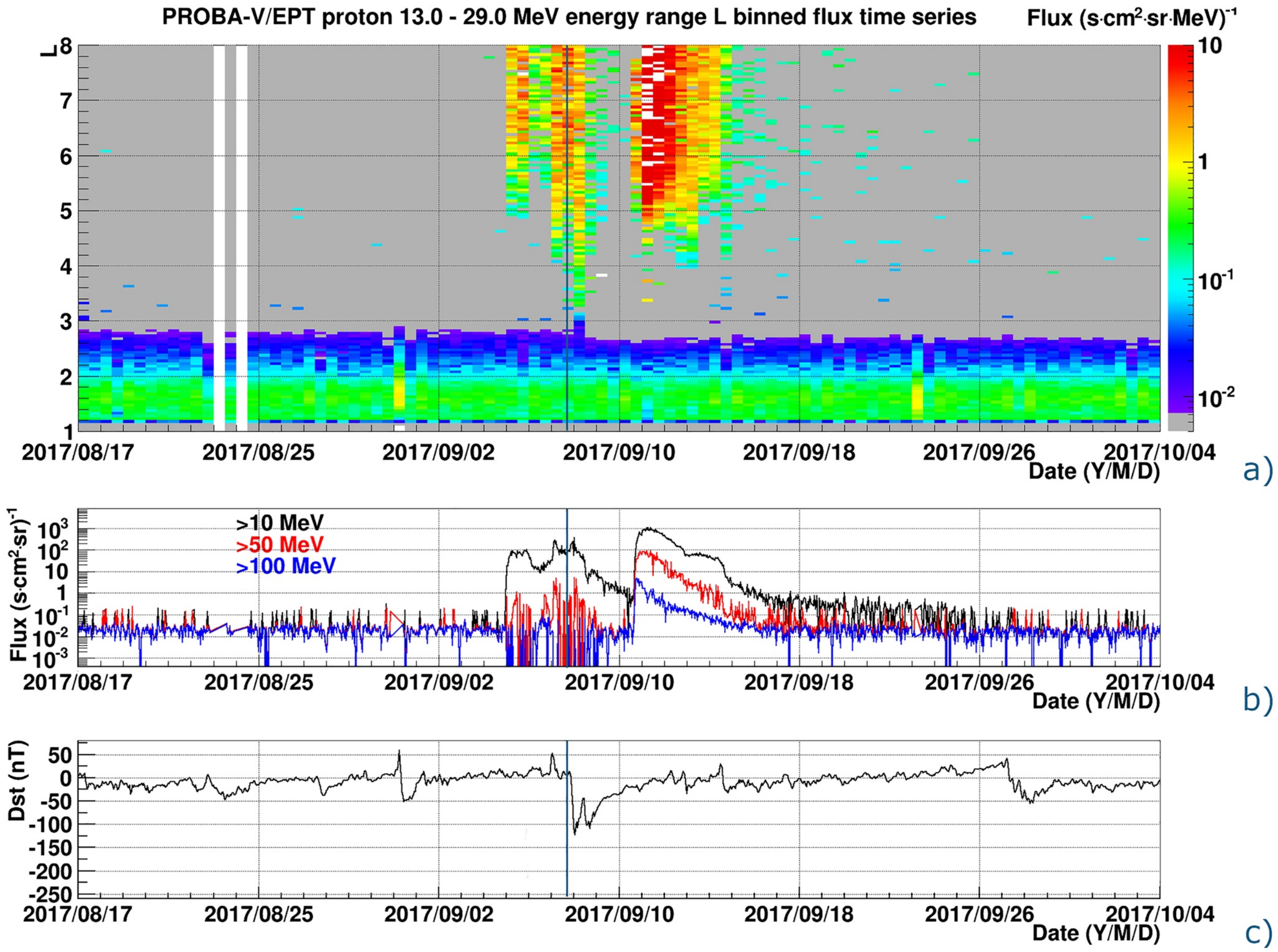

Figure 8. (a) Proton differential flux observed by EPT in Ch 2 (13–29 MeV) as a function of L and time from 17 August to 4 October 2017. The bin size in L is 0.05 and the bin size in time is 0.5 day. White regions signify that no data was available for those bins, either due to anomaly in satellite operation (white bands) or data filtering procedure (individual bins). (b) The EPT derived integral fluxes for protons of $E > 10$, >50 and >100 MeV and (c) the Dst variation for the same time period. A vertical blue line is drawn to facilitate the identification of occurrence of the Dst (geomagnetic) storm event with respect to the SEP event.

The SEP injection of protons at high L values started on 15 March 2015, thus a few days before the geomagnetic storm started, with a strong Dst decrease during the night from 16 to 17 March. The SEP injection did barely reach the $L = 4$ region. However, in combination with the onset of the storm, the reduction of the outer edge of the inner proton belt, decreasing suddenly from $L = 3$ to $L = 2.7$ associated to the compression of the magnetic field during the storm can clearly be identified.

A similar decrease of the outer edge of the proton belt is also seen during the event of September 2017 (Figure 8). Panel (a) shows that this SEP event is much more intense than the 2015 event and that even protons of energy >100 MeV are observed (Figure 8b). For the energies <30 MeV, SEP protons reach down to L $\sim$ 3. Once the interplanetary shock arrives at the spacecraft, the accelerated protons of the SEP seem even gain access to the inner belt. However, it does not last for long and when the second decrease in Dst occurs, the outer edge of the belt erodes to a level that is inside the original outer edge. Associated to the easier access of SEP protons at low L, inner belt protons are lost at its outer edge. This has been observed previously: depending on the magnetic perturbation and SEP injections, additional protons can be trapped in the inner belt or on the contrary protons can be lost (Selesnick et al., 2010). The limit of the magnetic trapping of the protons depends on the gyroradius of the protons that has to be sufficiently low to have a periodic motion (Maget et al., 2013). When the magnetic field is disturbed, non-adiabaticity and violation of the guiding center approximation can result in their loss (Pierrard et al., 2021). This is here observed at the outer edge of the proton belt, essentially for protons of Ch1 and Ch2, because their edge is at $L > 2.5$ and their fluxes are relatively high. In fact, the sensitivity in flux of EPT for higher

10.1029/2022JA031202

energies may be a reason that such phenomena cannot be observed for $E > 30$ MeV, yet it cannot be excluded that the depletion in flux as observed at higher L in Figure 3 comes from multiple erosion events occurring during solar declining phase and that annihilates somehow the flux increase due to changes in extension of the atmosphere, especially that those particles have the largest gyroradius.

Accordingly, such losses can be attributed to the disruption of the adiabatic particle motion due to distortion of the magnetic field, specifically by increase of the field line curvature. Such losses due to the magnetic field perturbation can happen even without significant SEP event, only due to geomagnetic storms that can be generated by other solar events not including energetic particles, like Corotating Interaction Regions (CIR) for instance (e.g., Rouillard et al., 2021 for a review). The maximum L of trapped protons, that is, the extension of the proton belt, can be related to the trapping limits estimated from magnetic field line curvature. Rapid magnetospheric compression can cause solar proton injections and radial shift of preexisting trapped protons (Selesnick et al., 2010).

For the two events shown here, it could be observed that the loss of radiation belt border protons was higher for the 2015 event than for the 2017 event, linked certainly to the higher intensity and hence compression within the 2015 storm.

6. Structures in the SAA at Low Proton Energies

Within this section a special feature observed at low proton energy <15 MeV will be emphasized.

Figure 9a shows 2-s resolution data taken along the orbit as a function of L for the region $1 < L < 6$ (all B included) during the time period 1/1/2014–31/3/2014. On this graph, the coverage of the 9.5–13 MeV protons of EPT (blue dots in top panel) is particular because it registered the presence of two peaks separated by a little dip around $L = 2$. This phenomenon is observed immediately after the launch of PROBA-V and during all the observation period, but only for this low energy channel. The points observed above $L = 4$ originate from a SEP event that occurred during January 2014.

The double peak is unexpected because it is not obtained by the AP8 model (Vette, 1991), as illustrated in the bottom panels of Figure 9 for maximum (panel b) and minimum (panel c) solar activity. These panels show the differential proton flux as a function of L as calculated from runs on SPENVIS (www.spenvis.oma.be/) for a helio-synchronous polar orbit at 820 km altitude, for different energies corresponding to those of EPT channels. Note that AP8 predicts omnidirectional integral fluxes, and hence the differential unidirectional (per steradian) fluxes are calculated from the AP8 model. The passage from integral to differential fluxes is simply done by linear interpolation and for the passage from omnidirectional to directional fluxes, an isotropic flux is assumed (division by $4\cdot\pi$ sr). No correction like suggested by Badhwar and Konradi (1990) for flux anisotropy was applied. The fluxes of EPT are also unfolded under the assumption of isotropic flux. Therefore, some difference in absolute height may appear, also due to the fact that the higher the proton energy in EPT, the lower the FOV within which the particles are detected, hence the somewhat higher fluxes observed for EPT with respect to AP8 based data.

Figure 9a suggests that there are two populations within the proton belt: (a) the population below $L = 2$ where the high energy protons are also significantly present and the proton spectra are relatively flat and (b) the population above $L = 2$ where the low energies below 10 MeV largely dominate and the proton spectra are rather steep. The origin may be either different source of particle production, different loss processes or a combination of both. More information about this is given in the discussion Section 7.

The second peak in Ch 1 (at $L > 2$) looks like an “additional” belt in the South part of the SAA, as illustrated in the map on Figure 10. In the top panel, corresponding to Ch 1, the South part of the SAA is more extended (see the red region that extends up to $L = 2.5$) than what is observed in higher energy channel (see bottom panel for Ch 2 in Figure 10). For the proton channel $E = 9.5$–13 MeV (upper panel), a slight valley can be observed in the region L ~ 2. For the proton channel $E = 13$–29 MeV, the flux in the region $L > 2$ has significantly decreased. The black lines show ascending trajectories of the EPT when traversing the SAA.

The particularity of the SAA southern region gets even more highlighted when looking at Figure 11. Note that this time, the analyzed data come from the period after recalibration of the EPT and therefore the channel 1 data is based on information when the protons has passed only through S1 and then hit S2. The statistics in the channel after 2 s integration time is very low and therefore the average is done over a longer period than for Figure 10,

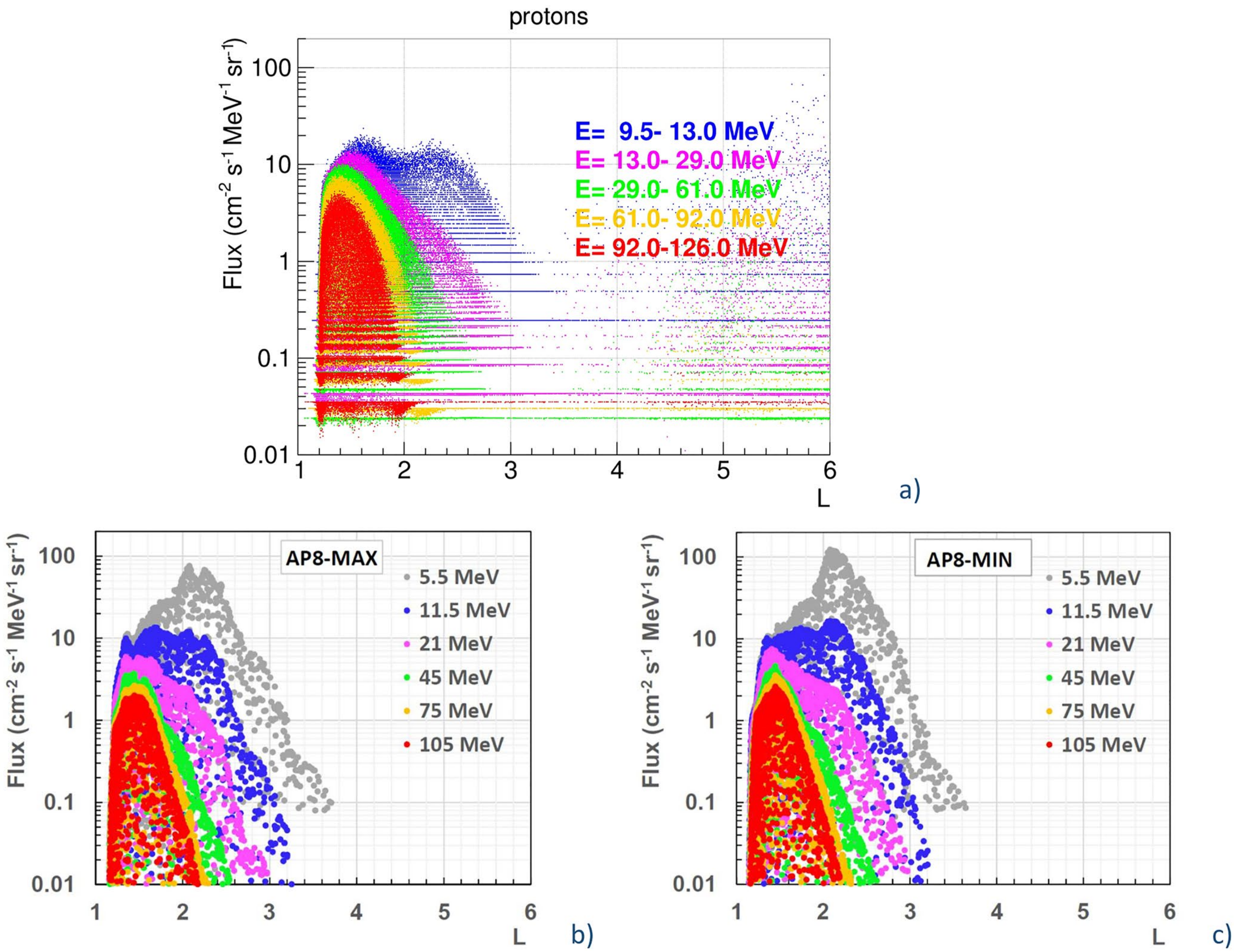

Figure 9. Top panel: Differential 2-s resolution proton flux as a function of L as observed by the EPT on-board PROBA-V (time period 1/1/2014–31/3/2014). Bottom panels: Differential proton flux as a function of L as result of the AP8-MAX (b) and AP8-MIN (c) model (Vette, 1991), from a run on SPENVIS for a helio-synchronous polar orbit at 820 km altitude.

that is, 2 months. Also, to get a coherent comparison, the S1 data were corrected (renormalized) to take into account the difference in FOV which is important when analyzing data in a region where the fluxes have a steep PAD (Borisov & Benck, 2019). Between January 2014 (top panel of Figure 10) and October/November 2014 (top panel of Figure 11), the situation has roughly not evolved. However, the layout of the SAA for channel 1 changes significantly from end 2014 (solar maximum, top panel) to end 2019 (solar minimum, middle panel of Figure 11), with the southern region getting a strong enhancement in low energy protons. A factor 3 is observed at the northern edge of the SAA and around $L = 2$ when comparing 2019 with 2014 (see red regions in Figure 11c). This increase is also visualized in Figure 12 where one (B, L) bin close to the valley has been chosen as illustration. This figure shows that the increase is continuous and not especially associated to specific events.

7. Discussion With Respect to Previous Observations

Earlier satellites had detected multiple proton belts in the nineties. SAMPEX showed the formation of several proton belts after the big SEP events of 1998 and 2000 (Lorentzen et al., 2002). CRRES observed that the March 1991 storm created a second, stable high energy belt above $L = 1.8$ for protons of 42 MeV, with peak flux values exceeding pre-storm values by an order of magnitude (Albert et al., 1998). Intense fluxes of low energy protons down to $L = 1.35$ were reported by Parsignault et al. (1981) from 1972 to 1976. ICARE on board SAC-C observed an increase of 10 MeV protons flux in the South part of the SAA clearly due to the 31 March 2001 SEP event

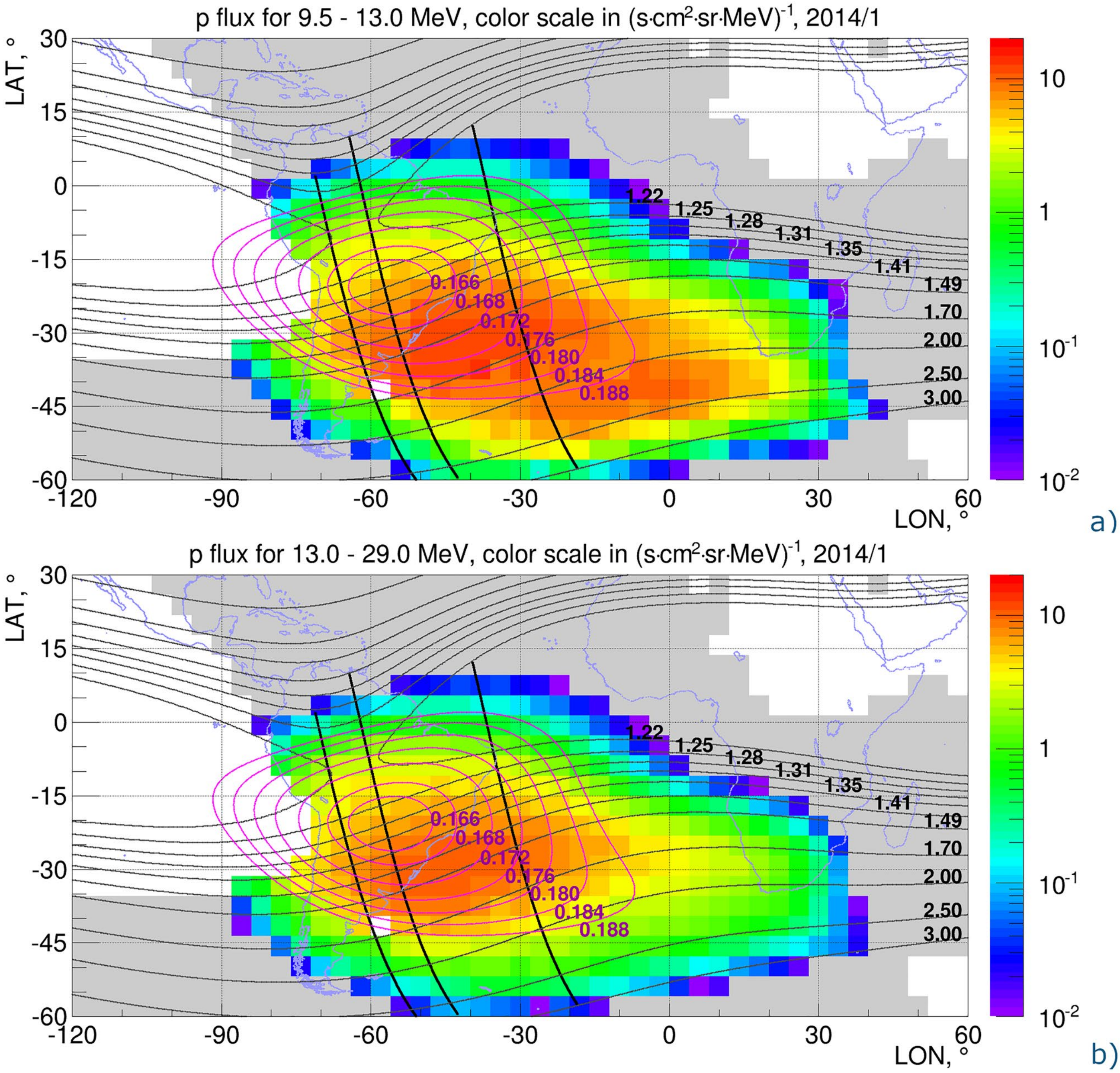

Figure 10. Geographical maps of the SAA, observed in January 2014 by EPT for two proton energies: Ch 1 (9.5–13 MeV, top panel) and Ch2 (13–29 MeV, bottom panel). Nightside data with boresight orientation 90° ± 10° were selected. Please refer to the caption of Figure 3 for explanations on color scale and lines.

(Falguere et al., 2002; Girgis et al., 2022). But it is the first time that multiple belts, associated to a splitting of the SAA, are observed at long term in this specific energy range and more recently at LEO. The advantage of EPT in comparison to other detectors at LEO is that it directly measures the differential flux in a set of channels with a good defined FOV. Since these small-scale structures may appear only for some specific energies, they cannot be easily detected in integral flux measurements. Observations in regions of high energy radiation are particularly complicated due to possible contaminations.

The NASA Van Allen Probes (VAP, also called Radiation Belt Storm Probes) mission (Mauk et al., 2012) has been launched in 2012 and operated simultaneously with EPT. The data sets of EPT and VAP allow to perform unprecedented studies of the radiation belt electron and proton variability in response to solar activity and during the same periods of time. The orbit of VAP is completely different from PROBA-V: VAP flied on a low inclination (10°) elliptical orbit ranging from 600 to 30,600 km with a period of 9 hr and traversing the inner belt very

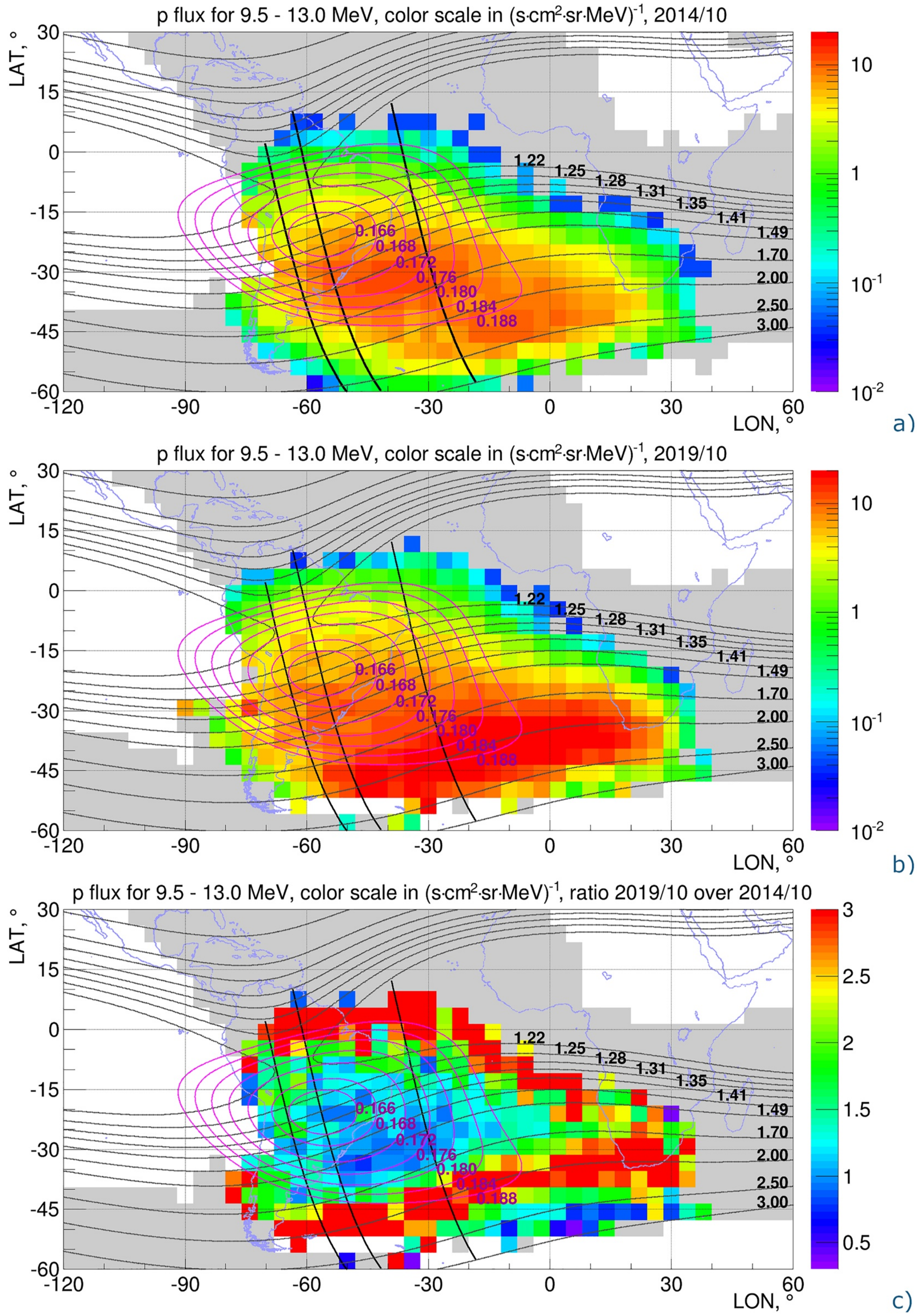

Figure 11. Geographical maps of the averaged proton flux in Ch 1: (a) October and November 2014, (b) October and November 2019, (c) ratio between 2019 and 2014 data. The bold black lines are parts of trajectories showing how EPT crosses the SAA during night passes from south to north. The gray areas are those where the fluxes are below minimum, that is, 10^{-2} s^{-1} cm^{-2} sr^{-1} MeV^{-1}, and the white areas are those where no data fulfill the selection criteria: night side data with boresight orientation 90° ± 10°. Iso-L lines and iso-B lines are shown by black and pink lines respectively.

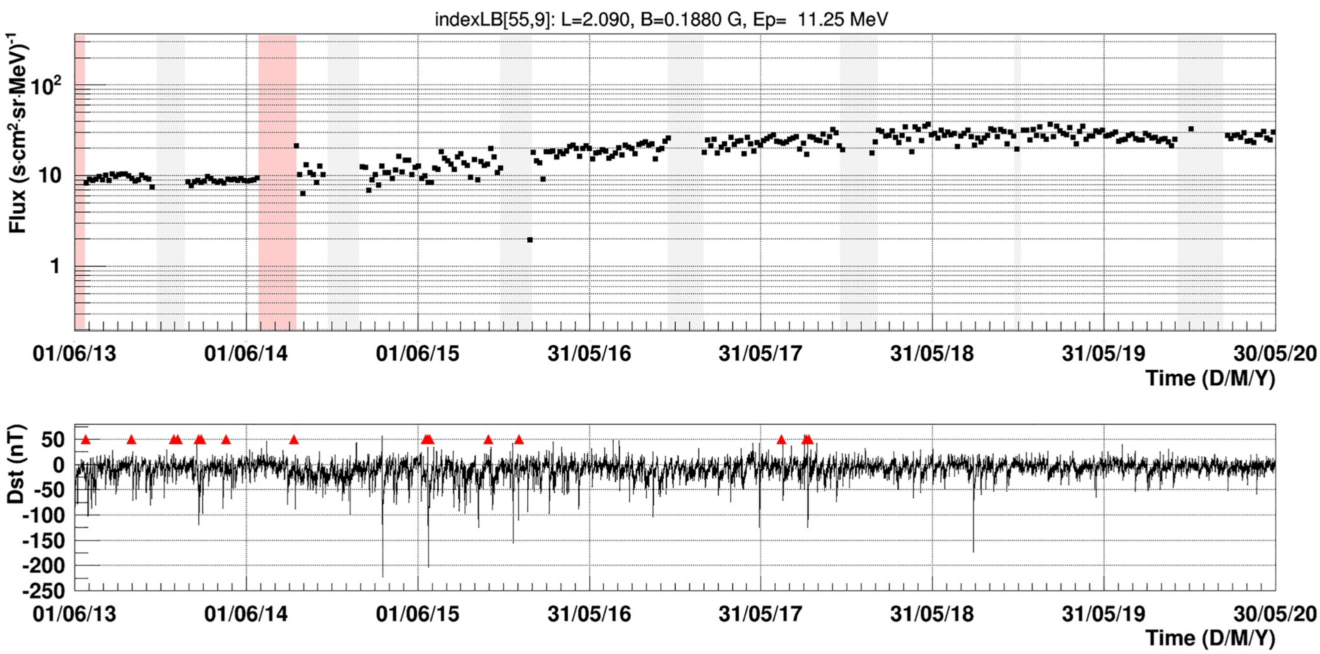

Figure 12. Time series of proton flux (weekly averages) in the SAA at one position in the southern part of the SAA: $L = 2.09 \pm 0.01$ and $B = 0.188 \pm 0.02$ G. The fluxes present night-side data with boresight orientation $90° \pm 10°$ (upper panel). The bottom panel shows Dst as a function of time and the red triangles indicate the occurrence of SEP events. The statistics in the flux data has changed after 15 September 2014 due to the change in FOV (change in detector configuration, please see text), hence the increased data spread.

quickly. Conjunction regions only exist at $L < 1.5$ (Pierrard et al., 2021). In addition to the different orbit, the proton energy channels of REPT (Relativistic Electron Proton Telescope) (Selesnick et al., 2016) ranging from 18 to 78 MeV are also different from EPT, complicating the direct comparison.

Close to the equatorial plane, the VAP/REPT fluxes for $E < 32$ MeV showed a two-peak structure evolving with time with a valley located around $L = 1.7$ (Selesnick & Albert, 2019). The fluxes observed by VAP/REPT decrease with time from October 2013 to August 2015 at $L < 1.6$ but increase at $L > 1.7$ corresponding to the second peak (see Figure 2 of Selesnick et al., 2016). An increase in flux at $L > 1.7$ is also seen in EPT but only significant (due to statistical uncertainty) when looking over a larger time frame (see Figure 11c southern part of the SAA for isolines $L > 1.7$).

In the study of Selesnick et al. (2016), REPT with its FOV of 32° was measuring protons with pitch angles around 90°, that is, the protons that mirror near the magnetic equator. Those protons were measured at high altitude except when $L < 1.5$ (possible conjunction region). On the other hand, EPT mainly measures protons that have small equatorial PA as only those can reach low altitude. The behavior of these protons may be different. For example, the equatorial mirroring protons measured by REPT at $L > 1.2$ are obviously not affected by solar cycle variation, that is, the atmospheric and ionospheric density. This is very different from measurements taken at highly inclined LEO like PROBA-V/EPT that shows variation with solar cycle, as also confirmed by SAMPEX or POES for instance (Li et al., 2020). Also, the observed flux variations are dependent on L and B.

8. Conclusions

Since May 2013, the EPT spectrometer on-board PROBA-V provides high-resolution proton flux measurements in the space environment of the Earth. In the present work, we analyze the long-term and short-term evolution of the proton fluxes for different energy ranges and determine the causes of the time variations to identify the mechanisms of sources and losses that influence their changes with time. Very few clean measurements of differential proton fluxes at LEO are available at different energy ranges above ~10 MeV during the last years. That is why EPT measurements provide new results in this field, such as the splitting of the SAA observed for the energy <15 MeV at LEO.

Indeed, only for Ch 1 (9.5–13 MeV), a stable double peak structure is observed by EPT with a gap at $L = 2$. This corresponds to a long-term splitting of the SAA in this energy range and a higher extension of the south part of the SAA. Such a long-term splitting of the SAA at LEO was never reported before and could be identified with the high-resolution measurements of differential fluxes made by EPT.

In addition, analysis of long-time variations showed an anti-correlation (although time-shifted) between the proton fluxes and the solar activity at all energies of EPT at the border of the SAA, most strongly observed at $L < 1.25$ and L ~ 2.1. The low flux at low L in 2014 (solar maximum) can be attributed to atmospheric loss at the lower edge of the proton belt. During the decreasing phase till the solar activity minimum in 2019, the fluxes slightly increase due to the lower extension of the atmosphere allowing to the protons to penetrate deeper. CRAND may also play a role, with different effects depending on the energy and the L-shell.

SEP events increase the fluxes at high L during a few days, but do not inject fluxes in the SAA during the period of observations of EPT (2013–2022). Nevertheless, the most intense geomagnetic storms decrease the extension of the inner belt, best observable at the lowest energies. This effect is particularly visible after the geomagnetic storm of March 2015 and the storm appearing a few days after the beginning of the September 2017 SEP event. The arrival of many of such storms during the declining phase of the solar cycle may compensate somehow the flux increase due to the favorable atmospheric conditions (lower atmospheric loss) when solar minimum approaches. This effect is observed to be energy dependent.

Data Availability Statement

EPT data are publicly available on the Space Situational Awareness website of ESA http://swe.ssa.esa.int/space-radiation. The list of the SEP events is available on https://umbra.nascom.nasa.gov/SEP/. Dst data was retrieved from https://wdc.kugi.kyoto-u.ac.jp/ and sunspot number data was downloaded from http://www.sidc.be/silso/datafiles/.

Acknowledgments

The project 21GRD02 BIOSPHERE has received funding from the European Partnership on Metrology, co-financed by the European Union's Horizon Europe Research and Innovation Programme and by the Participating States. This research was supported by the International Space Science Institute (ISSI) in Bern, through ISSI International Team project #477 (Radiation Belt Physics From Top To Bottom: Combining Multipoint Satellite Observations And Data Assimilative Models To Determine The Interplay Between Sources And Losses). All authors are grateful to the PROBA-V/EPT teams at B.USOC and ESA/Redu for their involvement in the data acquisition process. Sylvie Benck and Stanislav Borisov thank the Belgian Science Policy—Space Research and Applications (BELSPO) team for support to the PRODEX project entitled "PROBA-V/EPT—Data Exploitation-Extension," ESA/PRODEX PEA N° C4000107617. They also thank ESA/ESTEC members for their continuous support throughout the EPT mission and ESA/ESOC members for funding the first EPT products development within the Space Weather program (SSA—ESC—P2 and –P3) and its development continuation within the frame of ESA Space Safety Program's network of space weather service development and pre-operational activities (supported under ESA Contract 4000134036/21/D/MRP, the SWESNET project).

References

Albert, J. M., Ginet, G. P., & Gussenhoven, M. S. (1998). CRRES observations of radiation belt protons 1. Data overview and steady state radial diffusion. *Journal of Geophysical Research*, *103*(A5), 9261–9274. https://doi.org/10.1029/97JA02869

Ameri, D., & Valtonen, E. (2019). Potential role of energetic particle observations in geomagnetic storm forecasting. *Advances in Space Research*, *64*(3), 801–813. https://doi.org/10.1016/j.asr.2019.05.012

Amit, H., Terra-Nova, F., Lézin, M., & Trindade, R. I. (2021). Non-monotonic growth and motion of the South Atlantic Anomaly. *Earth Planets and Space*, *73*(1), 38. https://doi.org/10.1186/s40623-021-01356-w

Anderson, P. C., Rich, F. J., & Borisov, S. (2018). Mapping the South Atlantic Anomaly continuously over 27 years. *Journal of Atmospheric and Solar-Terrestrial Physics*, *177*, 237–246. https://doi.org/10.1016/j.jastp.2018.03.015

Badhwar, G. D., & Konradi, A. (1990). Conversion of omnidirectional proton fluxes into a pitch angle distribution. *Journal of Spacecraft and Rockets*, *27*(3), 350–352. https://doi.org/10.2514/3.26148

Baker, D. N., Erickson, P. J., Fennell, J. F., Foster, J. C., Jaynes, A. N., & Verronen, P. T. (2018). Space weather effects in the Earth's radiation belts. *Space Science Reviews*, *214*(1), 17–60. https://doi.org/10.1007/s11214-017-0452-7

Benck, S., Borisov, S., Cyamukungu, M., Evans, H., & Nieminen, P. (2016). Characterization of solar energetic H and He spectra measured by the energetic particle telescope (EPT) on-board PROBA-V during the January 2014 SEP event. *IEEE Transactions on Nuclear Science*, *63*(6), 2941–2949. https://doi.org/10.1109/TNS.2016.2610520

Borisov, S., & Benck, S. (2019). *Data analysis procedure for proba-V/EPT spectra acquired after 15/09/2014, technical Note 1B, issue B, review 1*. EPT-DEXT-TN-011-CS.

Borisov, S., Benck, S., Cyamukungu, M., O'Brien, P., Mazur, J., Nieminen, P., et al. (2014). Angular distribution of protons measured by the energetic particle telescope on PROBA-V. *IEEE Transactions on Nuclear Science*, *61*(6), 3371–3379. https://doi.org/10.1109/TNS.2014.2361951

Brekke, A. (2013). *The Earth's magnetic field and magnetosphere, Physics of the Upper Polar Atmosphere*. Springer. https://doi.org/10.1007/978-3-642-27401-5

Bruno, A., Martucci, M., Cafagna, F. S., Sparvoli, R., Adriani, O., Barbarino, G. C., et al. (2021a). East–West proton flux anisotropy observed with the PAMELA mission. *The Astrophysical Journal Letters*, *919*(6p), 114. https://doi.org/10.3847/1538-4357/ac1677

Bruno, A., Martucci, M., Cafagna, F. S., Sparvoli, R., Adriani, O., Barbarino, G. C., et al. (2021b). Solar-cycle variations of South Atlantic anomaly proton intensities measured with the PAMELA mission. *The Astrophysical Journal Letters*, *917*(6p), L21. https://doi.org/10.3847/2041-8213/ac1a74

Cabrera, J., & Lemaire, J. (2007). Using invariant altitude (h(inv)) for mapping of the radiation belt fluxes in the low-altitude environment. *Space Weather*, *5*(4), S04007. https://doi.org/10.1029/2006SW000263

Cyamukungu, M., Benck, S., Borisov, S., Bonnet, L., Grégoire, G., Cabrera, J., et al. (2014). The energetic particle telescope (EPT) on board PROBA-V: Description of a new science-class instrument for particle detection in space. *IEEE Transactions on Nuclear Science*, *61*(6), 3667–3681. https://doi.org/10.1109/TNS.2014.2361955

Falguere, D., Boscher, D., Nuns, T., Duzellier, S., Bourdarie, S., Ecoffet, R., et al. (2002). In-flight observations of the radiation environment and its effects on devices in the SAC-C polar orbit. *IEEE Transactions on Nuclear Science*, *49*(6), 2782–2787. https://doi.org/10.1109/TNS.2002.805380

Girgis, K. M., Hada, T., Matsukiyo, S., & Yoshikawa, A. (2021). Inner radiation belt simulations of the proton flux response in the South Atlantic Anomaly during the geomagnetic storm of 15 May 2005. *Journal of Space Weather Space Climate*, *11*, 48. https://doi.org/10.1051/swsc/2021031

Girgis, K. M., Hada, T., Matsukiyo, S., & Yoshikawa, A. (2022). Radiation analysis of LEO mission in the South Atlantic Anomaly during geomagnetic storm. *IEEE Journal of Radio Frequency Identification*, *6*, 292–298. https://doi.org/10.1109/JRFID.2022.3163441

Heynderickx, D., Kruglanski, M., Pierrard, V., Lemaire, J., Looper, M. D., & Blake, J. B. (1999). A low altitude trapped proton model for solar minimum conditions based on SAMPEX/PET data. *IEEE Transactions on Nuclear Science*, *46*(6), 1475–1480. https://doi.org/10.1109/23.819110

Jiggens, P., Clavie, C., Evans, H., O'Brien, T. P., Witasse, O., Mishev, A. L., et al. (2019). In situ data and effect correlation during September 2017 solar particle event. *Space Weather*, *17*(1), 99–117. https://doi.org/10.1029/2018sw001936

Kruglanski, M. (1996). Engineering tool for trapped proton flux anisotropy evaluation. *Radiation Measurements*, *26*(6), 953–958. https://doi.org/10.1016/S1350-4487(96)00097-2

Li, X., Selesnick, R., Schiller, Q., Zhang, K., Zhao, H., Baker, D. N., & Temerin, M. A. (2017). Measurement of electrons from albedo neutron decay and neutron density in near-Earth space. *Nature*, *552*(7685), 382–385. https://doi.org/10.1038/nature24642

Li, X., Selesnick, R. S., Zhao, H., Baker, D. N., Blake, J. B., & Temerin, M. A. (2021). Source, loss, and transport of energetic particles deep inside Earth's magnetosphere (L<4). In *Magnetospheres of the solar system*. In *Geophysical monograph series* (pp. 323–334). https://doi.org/10.1002/9781119815624.ch21

Li, X., Xiang, Z., Zhang, K., Khoo, L., Zhao, H., Baker, D. N., & Temerin, M. A. (2020). New insights from long-term measurements of inner belt protons (10s of MeV) by SAMPEX, POES, Van Allen Probes, and simulation results. *Journal of Geophysical Research: Space Physics*, *125*(8), e2020JA028198. https://doi.org/10.1029/2020JA028198

Lopez Rosson, G., & Pierrard, V. (2017). Analysis of proton and electron spectra observed by EPT/PROBA-V in the South Atlantic Anomaly. *Advances in Space Research*, *60*(4), 796–805. https://doi.org/10.1016/j.as.2017.03.022

Lorentzen, K. R., Mazur, J. E., Looper, M. D., Fennell, J. F., & Blake, J. B. (2002). Multisatellite observations of MeV ion injections during storms. *Journal of Geophysical Research*, *107*(A9), 1231. https://doi.org/10.1029/2001JA000276

Maget, V., Bourdarie, S., & Rolland, G. (2013). Characterizing solar energetic particles access to any earth-space location. *IEEE Transactions on Nuclear Science*, *99*(4), 1–7. https://doi.org/10.1109/TNS.2012.2233756

Mauk, B. H., Fox, N. J., Kanekal, S. G., Kessel, R. L., Sibeck, D. G., & Ukhorskiy, A. (2012). Science objectives and rationale for the radiation belt storm Probes mission. *Space Science Reviews*, *179*(1–4), 3–27. https://doi.org/10.1007/s11214-012-9908-y

McIlwain, C. E. (1966). Magnetic coordinates. *Space Science Reviews*, *5*, 585–598. https://doi.org/10.1007/BF00167327

Parsignault, A. M., Holeman, E., & Fizz, R. C. (1981). Long-term intensity decrease in the 8- to 25-MeV proton fluxes at low L values. *Journal of Geophysical Research*, *86*(A13), 11447–11450. https://doi.org/10.1029/ja086ia13p11447

Pierrard, V., Botek, E., Ripoll, J.-F., & Cunningham, G. S. (2020). Electron dropout events and flux enhancements associated with geomagnetic storms observed by PROBA-V/EPT from 2013 to 2019. *Journal of Geophysical Research: Space Physics*, *125*(12), e2020JA028487. https://doi.org/10.1029/2020JA028487

Pierrard, V., Lemaire, J., Heynderickx, D., Kruglanski, M., Looper, M., Blake, B., & Mewaldt, D. (2000). Statistical analysis of SAMPEX/PET proton measurements. *Nuclear Instruments and Methods in Physics Research*, *449*(1–2), 378–382. https://doi.org/10.1016/s0168-9002(99)01454-0

Pierrard, V., & Lopez Rosson, G. (2016). The effects of the big storm events in the first half of 2015 on the radiation belts observed by EPT/PROBA-V. *Annales Geophysicae*, *34*(1), 75–84. https://doi.org/10.5194/angeo-34-75-2016

Pierrard, V., Lopez Rosson, G., Borremans, K., Lemaire, J., Maes, J., Bonnewijn, S., et al. (2014). The energetic particle telescope: First results. *Space Science Reviews*, *184*(1), 87–106. https://doi.org/10.1007/s11214-014-0097-8

Pierrard, V., Lopez Rosson, G., & Botek, E. (2019). Dynamics of megaelectron volt electrons observed in the inner belt by PROBA-V/EPT. *Journal of Geophysical Research: Space Physics*, *124*(3), 1651–1659. https://doi.org/10.1029/2018JA026289

Pierrard, V., Ripoll, J.-F., Cunningham, G., Botek, E., Santolik, O., Thaller, S., et al. (2021). Observations and simulations of dropout events and flux enhancements in October 2013: Comparing MEO equatorial with LEO polar orbit. *Journal of Geophysical Research: Space Physics*, *126*(6), e2020JA028850. https://doi.org/10.1029/2020JA028850

Rouillard, A. P., Viall, N., Vocks, C., Wu, Y., Pinto, R., Lavarra, M., et al. (2021). In N.-E. Raouafi & A. Vourlidas (Eds.), *The solar wind, Book chapter in solar physics and solar wind, AGU monograph* (Vol. 1, pp. 1–33). https://doi.org/10.1002/9781119815600.ch1

Selesnick, R. S., & Albert, J. M. (2019). Variability of the proton radiation belt. *Journal of Geophysical Research: Space Physics*, *124*(7), 5516–5527. https://doi.org/10.1029/2019JA026754

Selesnick, R. S., Baker, D. N., Jaynes, A. N., Li, X., Kanekal, S. G., Hudson, M. K., & Kress, B. T. (2014). Observations of the inner radiation belt: CRAND and trapped solar protons. *Journal of Geophysical Research: Space Physics*, *119*(8), 6541–6552. https://doi.org/10.1002/2014JA02018

Selesnick, R. S., Baker, D. N., Jaynes, A. N., Li, X., Kanekal, S. G., Hudson, M. K., & Kress, B. T. (2016). Inward diffusion and loss of radiation belt protons. *Journal of Geophysical Research: Space Physics*, *121*(3), 1969–1978. https://doi.org/10.1002/2015JA022154

Selesnick, R. S., Hudson, M. K., & Kress, B. T. (2010). Injection and loss of inner radiation belt protons during solar proton events and magnetic storms. *Journal of Geophysical Research*, *115*(A8), A08211. https://doi.org/10.1029/2010JA015247

Siegl, M., Evans, H. D. R., DalySantin, E. J. G., Nieminen, P. J., & Bühler, P. (2010). Inner belt anisotropy investigations based on the standard radiation environment monitor (SREM). *IEEE Transactions on Nuclear Science*, *57*(4), 2017–2023. https://doi.org/10.1109/RADECS.2009.5994710

Stassinopoulos, E. G., Xapsos, M. A., & Stauffer, C. A. (2015). Forty-year "Drift" and change of the SAA. NASA/Technical MEMORANDUM–2015-217547.

Vette, J. I. (1991). The NASA/National Space Science Data Center trapped radiation environment model program (1964-1991). NSSDC/WDC-A-R&S 91-29.